Access to Ru(IV)-Ru(V) and Ru(V)-Ru(VI) Redox in Layered Li_7RuO_6 via Intercalation Reactions

Haifeng Li[1], Beata Taudul[2,3], Grant C. B. Alexander[1], Jue Liu[4], John W. Freeland[5], Marie-Liesse Doublet[2,3], Jordi Cabana[1,*]

[1]Department of Chemistry, University of Illinois at Chicago, Chicago, Illinois 60607, United States

[2]ICGM, Univ Montpellier, CNRS, ENSCM, 34090 Montpellier, France

[3]Réseau sur le Stockage Électrochimique de l'Énergie (RS2E) CNRS FR3459, 80039 Amiens Cedex, France

[4]Neutron Scattering Division, Oak Ridge National Laboratory, Oak Ridge, Tennessee 37830 United States

[5]Advanced Photon Source, Argonne National Laboratory, Lemont, Illinois 60439, United States

*corresponding author: jcabana@uic.edu

Abstract

The push to increase the capacity of oxides to store charge as Li-ion battery cathodes has challenged our knowledge of the boundaries of redox chemistry and its relationship to atomic structure. Layered phases with Ru are now classical models in the quest for refined theories. Current understanding dictates that the highest formal state that can be reached in them is Ru(V), after which activity centered at the oxide anions is triggered. Yet this picture is challenged by this investigation of the intercalation chemistry of Li_7RuO_6. Coupling structural and spectroscopic analysis with computational simulations, we show that Li_7RuO_6 is capable of highly reversible lithiation to Li_8RuO_6, through the Ru(V)/Ru(IV) couple. Yet Li_7RuO_6 can also undergo anodic Li deintercalation showing clear evidence of reversible formation of Ru(VI) with octahedral coordination, an unusual state that is not accessible in other layered oxides. The results highlighted the versatility of the Ru-O bond to undergo distinct redox transitions depending on the specific layered arrangements. They enrich our understanding of redox chemistry in solids, while underscoring the need for descriptions of charge compensation that reflect the nuance of covalent interactions.

1. Introduction

The Li-ion battery, which stores charge through the shuttling of Li^+ ions between two electrodes, significantly accelerated the realization of our wireless society by powering the portable electronic devices.[1, 2] Nowadays, they are increasingly central to a sustainable and clean-energy based society by enabling the substitution of fossil fuels by renewable sources, through their growing implementation in electric vehicles (EVs) and grid applications.[3-5] In order to realize their full potential, intense research continues to further increase the energy density of the device, which is currently handicapped by the lower capacity of the oxide cathodes compared to the anode.[6]

Conventionally, cathodes store energy through (de)intercalation reactions of Li accompanied by changes in redox occurring on the transition metal (TM) centers (cationic redox, CR), with the metrics of capacity being determined by the number of transferred electrons in the reaction.[7, 8] Practically, there are limits to how much a TM center can be oxidized before the oxide becomes unstable and the reaction becomes irreversible, leading to a loss in cycle life of the battery. As a classical example, the first commercial cathode, $LiCoO_2$, possesses a high theoretical capacity of 274 mAh/g for a full 1-electron oxidation of Co(III), but, in practice, it can only be cycled at a maximum capacity of ~165 mAh/g to avoid inducing structural instability and severe capacity fade.[9-12] The tradeoff between stability and storage capacity places emphasis on the challenge to define the fundamental limits of redox chemistry in transition metal oxides.

One way to increase the exhibited capacity is to design materials with multielectron transitions in TMs without crossing their highest known stable states, which is exemplified in the full leveraging of the Mn(II)/Mn(IV) redox couple by Lee et al. in oxyfluorides with anion and cation disorder.[13] A second strategy has consisted in pushing the limits of redox to tap into the activity

of the oxide anions themselves, referred to as lattice oxygen redox (LOR) reactions, where non-bonding, and labile O 2p orbitals can be depopulated while reasonably preserving the reversibility of the framework.[14] This reactivity has now been widely reported in a variety of oxides with both ordered (layered) and disordered rocksalt frameworks, such as $Li_2Ru_{0.75}Sn_{0.25}O_3$[15], $Li_{1.17}Ni_{0.21}Co_{0.08}Mn_{0.54}O_2$[16], β-$Li_2IrO_3$[17], $LiNi_{1/3}Co_{1/3}Mn_{1/3}O_2$[18], $Li_{1.3}Nb_{0.3}Mn_{0.4}O_2$[19], $Li_{1.3}Mn_{0.4}Ta_{0.3}O_2$[20], and $Li_{1.15}Ni_{0.35}Ti_{0.5}O_{1.85}F_{0.15}$[21], even with Na instead of Li, such as $Na_{0.6}[Li_{0.2}Mn_{0.8}]O_2$[22] and $Na_{0.5}Mg_{0.15}Al_{0.2}Mn_{0.65}O_2$[23]. The most compelling example of the potential of LOR to challenge conventions of redox chemistry is Li_3IrO_4, which is enabled by the existence of non-equivalent O sites with non-bonding O 2p orbitals whose depletion is subsequently stabilized by the highly covalent interaction between Ir and O.[24, 25] The challenge with LOR remains to induce it in less heavy and precious metals in a manner that reaches transformational capacities while being fully reversible, both in chemical pathways and energy efficiency. The delineation between conventional CR and LOR is also the object of ongoing debate. While oxides like $LiCoO_2$[12, 26] or $LiNi_{0.8}Co_{0.15}Al_{0.05}O_2$[27] could nominally be classified under CR, spectroscopic evidence suggests that O bears a role in charge compensation at high levels of oxidation, which has led some to invoke LOR. As the reverse example, while it is generally reported that the abnormal capacity displayed by Li_2MnO_3 is due to LOR accompanied by irreversible O_2 evolution,[28-30] Radin et al. proposed an alternative mechanism involving the Mn^{4+}/Mn^{7+} redox.[31]

Rocksalt-type ruthenium oxides are arguably the family that has attracted the most attention in recent years when defining the boundaries of reversible redox chemistry upon Li deintercalation.[15, 32-36] The layered honeycomb oxide Li_2RuO_3 was at the center of the first report of reversible LOR without irreversible evolution of O_2.[15, 33, 37] Measurements of X-ray absorption spectroscopy (XAS)

probed the changes at both Ru and O.[38, 39] The compound is reported to undergo CR (Ru(IV) to Ru(V)) to form $LiRuO_3$, but a reductive coupling mechanism of LOR takes place upon additional delithiation. Via computational methods, Xie *et al.* reported that the number of O 2p states accessible for LOR relies on an increasing O/TM ratio.[40] This prediction, so far, has been validated in Li_3TMO_4 where TM = Ir or Ru, which exhibit very large capacity upon oxidation.[24, 35, 36, 41] XAS indicated minimal changes at Ru(V) centers in both layered and disordered rocksalt polymorphs of Li_3RuO_4, while the density of unoccupied O states significantly increased.[36] This LOR mechanism upon delithiation unlocked a conventional path for cationic Ru(V)/Ru(IV) redox in $Li_{3-x}RuO_4$ (x = 1) upon subsequent reduction through relithiation, inducing chemical hysteresis. It is intriguing that a mechanism of CR via the Ru(V)-Ru(VI) couple does not seem to be accessible in any of these oxides, whereas K_2RuO_4 is a stable oxide with spectroscopic signatures clearly indicative of high valent Ru(VI).[42] It was recently proposed that low coordination environment (e.g., tetrahedral) around Ru centers plays a role in promoting such high formal oxidation states.[42]

So far, there is no experimental report of Li-rich compounds with O/TM ratio higher than 4 that exhibit clear evidence of high valent redox, which requires simultaneous insights from XAS at both cationic and anionic centers. The search for the highest O/TM ratio guided us toward Li_7RuO_6, which is again an ordered rocksalt with a layered arrangement where Ru is octahedrally coordinated.[43, 44] In this report, we studied its electrochemical properties, characterized the states involved in different reactions, and compared measurement of electronic structure with computations of the corresponding XAS. Unlike other Ru(V) counterparts, Li_7RuO_6 shows clear evidence of a highly reversible formation of Ru(VI) upon delithiation while preserving an octahedral environment. In contrast, like other layered rocksalts, Li_7RuO_6 can tap into the Ru(V)/Ru(IV) couple by filling the interlayer spacing. This finding indicates that accessing Ru(VI)

is not exclusively limited to frameworks with large alkali metal cations reported previously.[42] The comparison with other Ru(V) oxides highlights the versatility of the Ru-O bond to undergo distinct redox transitions depending on the specific layered arrangements in an ordered rocksalt. This report enriches our understanding of redox chemistry in solids, while underscoring the need for nuanced descriptions of the electronic states involved that reflect the nuance of covalent interactions.

2. Experimental section

2.1 Synthesis

Li_7RuO_6 was synthesized via a solid-state reaction from RuO_2 (Sigma-Aldrich, 99.9%) and a 10% stoichiometric excess of Li_2O (Sigma-Aldrich, 99.9%). The reactants were homogeneously ground by agate mortar and pestle, and pelletized. The pellets were transferred to an alumina crucible and heated at 950℃ for 20 hours in O_2 flow. After cooling to room temperature naturally, the as-obtained sample was ground into a fine powder and stored in the argon-filled glovebox for measurements.

2.2 Characterization

2.2.1 Electrochemical Testing

The electrochemical tests were carried out under galvanostatic conditions in Swagelok-type cells. Li_7RuO_6 is very sensitive to ambient conditions, so electrodes were built of loose powders using a rigorously dry process. In this process, the positive electrode materials were uniformly hand-mixed with 10wt% carbon black (Denka) for 10 min in argon-filled glovebox prior to cell assembling. All the mixing and fabrication of cells was conducted in an argon-filled glove box with moisture and oxygen levels of lower than 0.1 ppm. A piece of high-purity lithium foil (Alfa Aesar) was employed as both counter and pseudo-reference electrode, and a solution of 1 M $LiPF_6$

dissolved in a mixture of ethylene carbonate (EC)/ethyl methyl carbonate (EMC) in 3:7 weight ratio (Novolyte Technologies) was employed as the electrolyte. One disk of Whatman GF/D borosilicate glass fiber was employed as separator. The loading of powdered active material was 10 mg in a typical cell. The galvanostatic cycling was performed at room temperature using a VMP3 multipotentiostat (Bio-Logic) with a current rate of C/15 (defined as 1 Li extracted in 15 hours) with two cutoff voltage windows of 2.6-3.68 V and 1.5-2.6 V. Cycled samples from the Swagelok cells were recovered for *ex situ* characterization by disassembling the cells inside the glovebox, washed thoroughly with anhydrous DMC and dried under vacuum.

2.2.2 Structural Characterization

Ex situ high resolution synchrotron X-ray diffraction (SXRD) measurements were conducted at the 11-BM-B beamline at the Advanced Photon Source (APS) at Argonne National Laboratory (ANL) via a 12-channel analyzer detector array, with an average wavelength of 0.412795 Å produced by two platinum-striped collimating mirrors and a double-crystal Si(111) monochromator. The data was collected with a step size of 0.001° (2θ) and a scan speed of 0.01°/s. The powder samples were mixed with an appropriate amount of amorphous silicon dioxide to reduce X-ray absorption. Air-sensitive samples for *ex situ* measurements were sealed in Kapton capillaries with a diameter of 0.80 mm in an Ar-filled glovebox, and subsequently packed into heat-sealed Al-coated plastic bags for transport to the instrument. The capillaries were transferred out of the bag right before their measurement to minimize their exposure to air to the time required for the measurement. Time of flight neutron powder diffraction (TOF-NPD) data were collected at room temperature at the beamline 11A (POWGEN) of the Spallation Neutron Source (SNS) at Oak Ridge National Laboratory (ORNL) with the center wavelength of neutrons of 1.5 Å. An appropriate amount of sample was sealed in airtight vanadium sample cans with an inner diameter

of 6 mm under argon and transferred to the beamline station. Rietveld Refinements were performed through the GSASII program.[45]

2.2.3 X-ray Absorption Spectroscopy

Ex situ O K-edge X-ray absorption spectroscopy (XAS) was collected at the 4-ID-C beamline at the APS. Data were obtained at a spectral resolution of ~0.2 eV, under both total fluorescence yield (TFY) and total electron yield (TEY) modes. Harvested samples were stored in an Ar-filled glovebox, transferred into a portable transport container and then into the instrument antechamber under an Ar environment to minimize the potential exposure to air. During the measurement, three scans were performed on each sample, at each absorption edge, and scans were averaged to maximize the signal-to-noise ratio. The O K-edge was calibrated to a Sr_2RuO_4 reference measured simultaneously with the sample.

Ex situ Ru K-edge XAS was collected at the 20-BM-B beamline at the APS in transmission mode using a Si (111) double crystal monochromator. A standard foil of Ru metal located in front of a reference ion-chamber for Ru K-edge was measured simultaneously with each spectral sample for energy calibration. The energy threshold E_0 of the reference Ru foil was determined from the first derivative peak of the spectrum, and all XAS reference spectra were calibrated and aligned to the standard Ru energy for further comparison study. The background subtraction, X-ray absorption near edge spectroscopy (XANES) normalization and (extended X-ray absorption fine structure (EXAFS) fitting were carried out using IFEFFIT-based Demeter package.[46]

2.2.4 DFT calculations

Structural relaxation and electronic structures

Spin-polarized density functional theory (DFT) calculations as implemented in VASP (Vienna ab initio simulation package)[47, 48] were performed, using the projected augmented wave method (PAW)[49]. The generalized gradient approximation of Perdew−Burke−Ernzerhof (PBE)[50] in conjunction with the rotationally invariant Dudarev method (DFT + U)[51] were used to describe correlated d-electrons. Different U values were applied for Ru(d) metals (U=2 and 4 eV), leading to similar unit cell parameters. The average potentials computed with U=4 eV led to potential values closer to the experimental ones.

All input structures were relaxed until the forces on atoms are smaller than 2.10^{-3} eV/Å. The cut-off value for energy was set to 600 eV and the k-point mesh for Brillouin zone integration was converged to a grid density of at least 1000/at. In Li_8RuO_6 and Li_7RuO_6 structures, Li resides in octahedral and tetrahedral sites. Therefore, various Li distributions were considered for the delithiated structures with lithium removed either form Li_O or Li_T sites. The lowest energy structure for the hypothetical Li_5RuO_6 stoichiometry belongs to the $C_{2/m}$ space group.

XAS simulation

The XAS spectra were computed for all structures using the OCEAN code.[52, 53] OCEAN solves the Bethe-Salpeter equation (BSE)[54] based on the ground-state charge density and wave function obtained from the DFT-based Quantum Espresso (QE) program package,[55] using the local-density approximation (LDA or LDA+U)[56, 57] in conjunction with norm-conserving pseudopotentials.[58] To solve the Kohn-Sham equations, the cut-off value for the basis functions was set to 90 Ry and the k-point grid for the electronic density was converged with increasing k-point grids. The ground state calculations with QE were performed both in spin-polarized and spin non-polarized calculations to assess possible impact of Ru magnetization on the resulting XAS spectra. As for VASP calculations, Hubbard correction was added to Ru d-electrons (U=4 eV). BSE was solved

using 500 unoccupied bands and 800 bands were used to build the screened core-hole potential with the default k-point grid. Only dipole-allowed transitions were considered in the XAS calculations. The photon polarization vectors were set at [100], [010], and [001], and the final spectrum of each structure was obtained by averaging the spectra over all polarization vectors and individual oxygen atoms. Absolute excitation energy is not available from the calculations and ad hoc shift was applied to the simulated spectra for a sake of comparison with experimental data.

3. Results and Discussion

3.1 Structural Characterization of Li_7RuO_6

Li_7RuO_6 belongs to an extended family of lithium hexaoxometalates displaying a triclinic framework with space group $P\bar{1}$.[43] Rietveld refinement of high resolution SXRD and TOF-NPD was performed (Figure 1 and Table 1). The analysis revealed the existence of very small diffraction peaks attributed to tiny impurities of Li_3RuO_4 and Li_2O, in addition to a phase that could not be identified (Figure S1), which were also observed in previous reports.[43] Within the structure, O atoms pack into a slightly distorted hexagonal closed packing (hcp). Ru occupies octahedral sites in transition metal layers, and, within the layers, the RuO_6 octahedra are connected to each other via highly distorted $Li(4)O_6$ octahedra and disordered cationic vacancies (Figure 1c). The Ru adopts a slightly distorted environment with average two short, two intermediate and two long Ru-O distances of 1.968(5), 1.969(4), and 1.993(4) Å, respectively, with Ru displaced from the octahedron center. Li(1), Li(2) and Li(3) atoms fill half of the tetrahedral interstices between the resulting slabs $[Li(4)_{1/3}Ru_{1/3}\square_{1/3}O_2]$ (□ represents vacancies), leading to a double-layer sheet with edge-shared $(Li(1\text{-}3)O_4)$ tetrahedra.

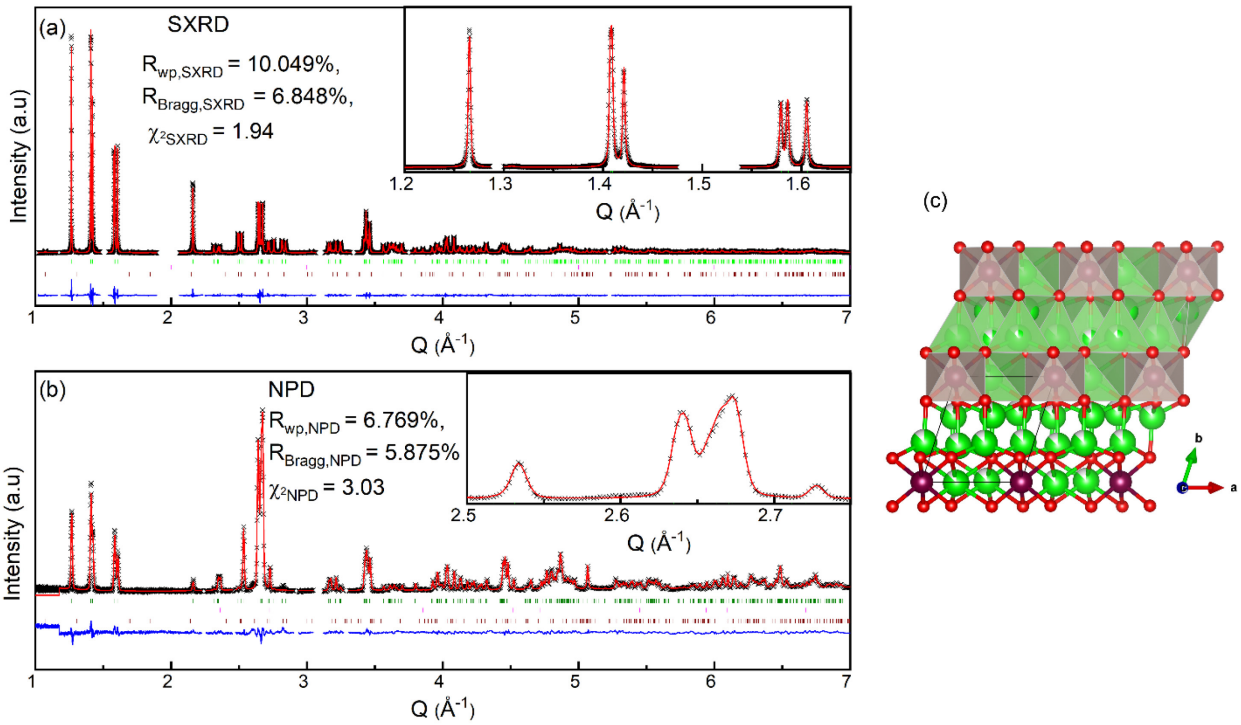

Figure 1. Rietveld refinement of SXRD (a) and NPD (b) patters of pristine Li_7RuO_6. The black crosses, and red solid line, correspond to experimental and calculated patterns, respectively. The blue solid line represents different patterns between experimental and calculated ones. Vertical green, pink, and purple bars dictate Bragg reflections of Li_7RuO_6, Li_2O, and Li_3RuO_4, respectively. The unknown phase was excluded during the refinement. The insets display zooms at different ranges to highlight the splitting of peaks due to the low triclinic symmetry. (c) Structure of pristine Li_7RuO_6. O, Ru, and Li are in red, purple, and green, respectively. Both polyhedral and ball-and-stick depictions are presented to maximize the visibility of the structural features.

Table 1. Crystallographic parameters and reliability factors extracted from the Rietveld refinement of SXRD and NPD for Li_7RuO_6.

Li_7RuO_6						
Space group: $P\bar{1}$; a = 5.3652(19) Å; b = 5.8604(17) Å; c = 5.3511(18) Å; α = 117.1727(28)°; β = 119.1111(31)°; γ = 62.6490(29)°; V = 124.531(3) $Å^3$						
Atom	Wyckoff position	x	y	z	Uiso ($Å^2$)	Occupancy
Ru1	1a	0.000000	0.000000	0.000000	0.0126(7)	1.000
O1	2i	0.9040(7)	0.2321(7)	0.3672(7)	0.0154(7)	1.000
O2	2i	0.2170(7)	0.2329(6)	0.0764(7)	0.0165(7)	1.000
O3	2i	0.3728(7)	0.7741(7)	0.2349(7)	0.0156(6)	1.000
Li1	2i	0.505(4)	0.370(4)	0.105 (4)	0.049(4)	0.8750
Li2	2i	0.1064(22)	0.6232(23)	0.2251(24)	0.0149(19)	0.8750
Li3	2i	0.7494(28)	0.6556(32)	0.4987(31)	0.0351(30)	0.8750
Li4	2i	0.651(5)	0.0091(32)	0.326(5)	0.054(4)	0.8750
Goodness-of-fitting parameters: $R_{WP, SXRD}$ = 11.173%; $R_{B, SXRD}$ = 7.509%; χ^2_{SXRD} = 2.05; $R_{WP, NPD}$ = 6.769%; $R_{B, NPD}$ = 5.875%; χ^2_{NPD} = 2.98.						

3.2 Voltage cutoff window of 2.6-3.68 V

Similar to our previous report of Li_3RuO_4,[36] the electrochemical properties of Li_7RuO_6 were evaluated within two separate windows: 2.6-3.68 V and 1.5-2.6 V vs Li^+/Li^0. In the first window, the initial oxidation of Li_7RuO_6 was carried out, to explore the following hypothetical reaction:

$$Li_7RuO_6 \rightarrow Li_6RuO_6 + Li^+ + e^- \quad (1)$$

Meanwhile, the reduction of Li_7RuO_6 was the initial step in the latter voltage window, corresponding to the following hypothetical reaction:

$$Li_7RuO_6 + Li^+ + e^- \rightarrow Li_8RuO_6 \quad (2)$$

Starting with a step of oxidation, the electrochemical cell displayed a long plateau at around 3.1 V, corresponding to a capacity equivalent to 0.7 mol Li per mol compound (Figure 2a). The differential capacity curve showed a sharp process centered at 3.1 V and a small shoulder at higher potential (Figure 2b). Further oxidation proceeded via a plateau at ~3.67 V that proceeded for a duration that was unreasonable under the assumption of a deintercalation mechanism (Figure S2). For the purposes of evaluating reversibility, an experiment was reversed after an accumulation of capacity equivalent to ~1.3 mol Li per mol Ru (Figure 2a). In these conditions, the reverse reduction consisted of a steep voltage drop and a comparably small plateau at 2.9 V (Figure 2a) corresponding to a sharp peak in the differential capacity plot (Figure 2b). During the reduction, 0.5 mol Li per mol compound was reinserted. In addition, the disappearance of the 3.68 V plateau demonstrated an electrochemical irreversibility at high voltage. Indeed, when charging was allowed to proceed beyond 3.7 V, there was a sharp voltage fall with a substantial capacity loss during reduction (Figure S2). Clearly, excessive charging leads to an irreversible process that destroys the function of the oxide. In contrast, the presence of the 2.9 V plateau reflects a reasonable reversibility with a modest hysteresis in potential (Figure 2c). Evaluation of sustained reversibility was conducted in an electrochemical experiment with a constrained cutoff voltage of 3.4 V (Figure 2c). Upon subsequent cycling, the electrochemical profile underwent a gradual disappearance of the reversible plateaus to lead to a sloping shape upon charge and the total capacity diminished (Figures 2a and c).

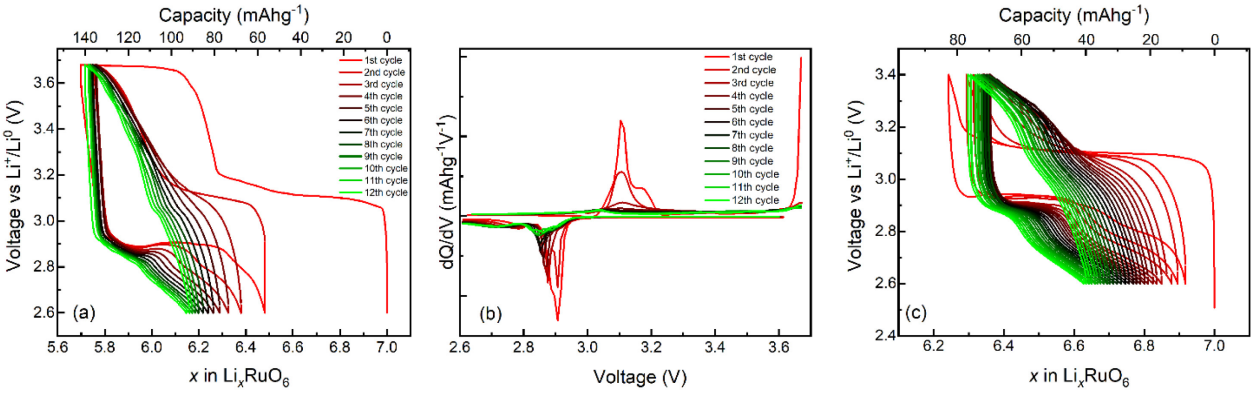

Figure 2. (a) Voltage-composition profiles of Li_7RuO_6 in the voltage window of 2.6-3.68 V and (b) the corresponding differential capacity plots. (c) Evolution of the profiles by constraining the charge cutoff to 3.5 V.

Ex situ SXRD data were collected at different states of charge (Figure 3). Oxidation to 3.4 V brought about new Bragg peaks, suggesting a variation in the crystal symmetry and likely a change in volume of the unit cell. The peak broadening and loss of intensity associated with the extraction of Li reflected a decrease in crystallinity. Unfortunately, a refinement of the powder diffraction data was not possible because no structural model could be found in the literature that could provide the basis for a refinement, even after unconstrained searches of the Inorganic Crystal Structure Database. Nonetheless, a Le Bail fit of the major reflections in the SXRD pattern was possible using a 1*1*2 supercell of the pristine state, still with $P\bar{1}$ space group (Figure S3 and Table S1). Some peaks remained too poorly fit to allow further analysis with the current data. Given the absence of a reliable initial model, the most modern approaches of structure searches combined with DFT are likely to be needed to solve this structure, as were showcased very recently by Mattei et al.[59]

The structure of the electrode harvested at 3.68 V resembled the previous state, without a shift of peak positions, except a subtle broadening of the peaks and a small reduction in peak intensity, implying a minimal loss in the crystallinity related to this additional process. The subsequent reduction largely restored the reflections of the pristine state, indicating a reversible process, but with a minor reduction in the peak intensity and some peak broadening, suggesting a permanent decrease in crystallinity from the electrochemical reactions (Figure S4). The SXRD data collected after the 2nd cycle demonstrated the same evolution of patterns as the first cycle (Figure 3b), further supporting a reversible (de)intercalation process.

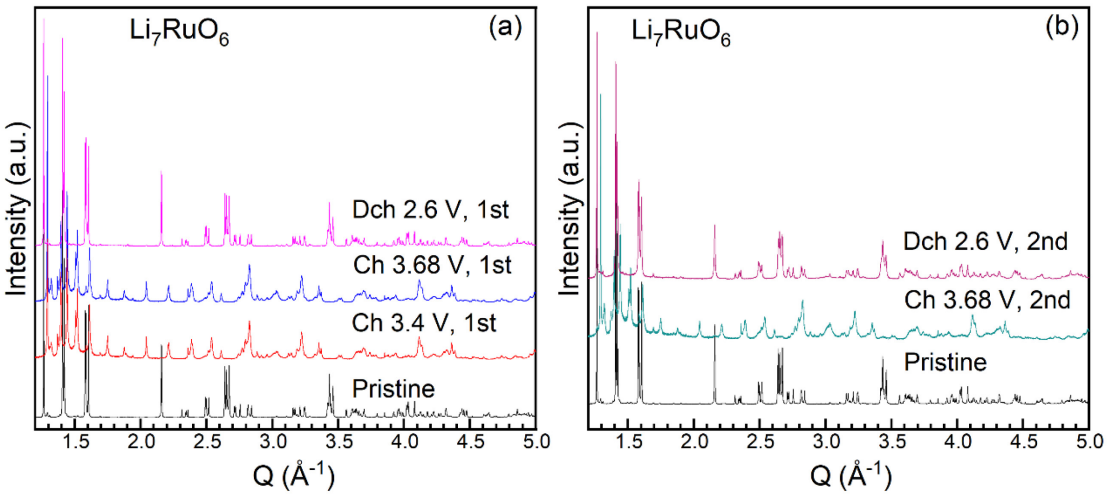

Figure 3. Stacked e*x situ* SXRD patterns of Li_7RuO_6 upon (a) the first and (b) the second charge and discharge in the voltage window of 2.6-3.68 V. Versions without offset are available in the Supporting Information.

Ex situ Ru K-edge XANES spectroscopy was performed for Li_7RuO_6 samples at different states of charge to gain insight into charge compensation. The first derivative of the spectrum was used to establish the position of the absorption edge, using the first inflection point above 22120

eV. This inflection point was considered to reflect the position of the main absorption edge, which, in turn, is affected by the formal oxidation state. An oxidation state of Ru(V) was assigned to pristine Li_7RuO_6 by comparing with the Ru K-edge XANES of $Ru^{IV}O_2$ and $Li_3Ru^{V}O_4$ (Figure S5). No obvious pre-edge features were observed. These features arise from dipole-forbidden 1*s*→4*d* transitions, but they can be enhanced in the presence of distortions of the octahedral environment that eliminate its inversion center, thus promoting the mixing between 4*d* and 5*p* orbitals. The absence of an obvious pre-edge peak in Li_7RuO_6 indicates that the distortion induced by a displacement of Ru off the center of the RuO_6 octahedra did not appear to meaningfully promote such mixing. Accordingly, the corresponding Ru K-edge EXAFS oscillations could be satisfactorily fit with undistorted RuO_6 octahedra with a Ru-O distance of 1.96 Å and a coordination number around 6 (Figure S6 and Table S2).

Upon the initial oxidation of Li_7RuO_6 to 3.4 V, the absorption rising edge underwent a shift by (+0.7 eV) relative to the pristine state (Figure 4), clearly reflecting the oxidation of Ru, but with a final oxidation state slightly lower than (VI) based on the comparison with reference $K_2Ru^{VI}O_4$ (Figure S7).[35] This observation is consistent with the fact that less than 1 mol electrons were removed per mol compound. However, it is important to note that such oxidation was not accompanied by the onset of a pre-edge peak, as would be expected if Ru migrated to a tetrahedral environment because it does not have an inversion center. Indeed, such pre-edge is observed in $K_2Ru^{VI}O_4$ (Figure S7). Indeed, the only changes observed in the EXAFS analysis were a decrease in the Ru-O distance to 1.92 Å, maintaining a coordination number consistent with RuO_6 octahedra (Figure S6 and Table S2). Further oxidation to 3.68 V did not affect either the position of the absorption edge or the pre-edge intensity in comparison with the previous state, indicating that Ru did not directly participate in the reactions occurring at this potential. The reverse reduction shifted

the rising edge back to lower energy to closely approach the pristine state (Figure 4). The EXAFS oscillations also reverted to the initial state, with a Ru-O distance of 1.96 Å and a coordination number around 6 (Figure S6 and Table S2). Overall, the results demonstrate the reduction of Ru upon discharge with very high efficiency.

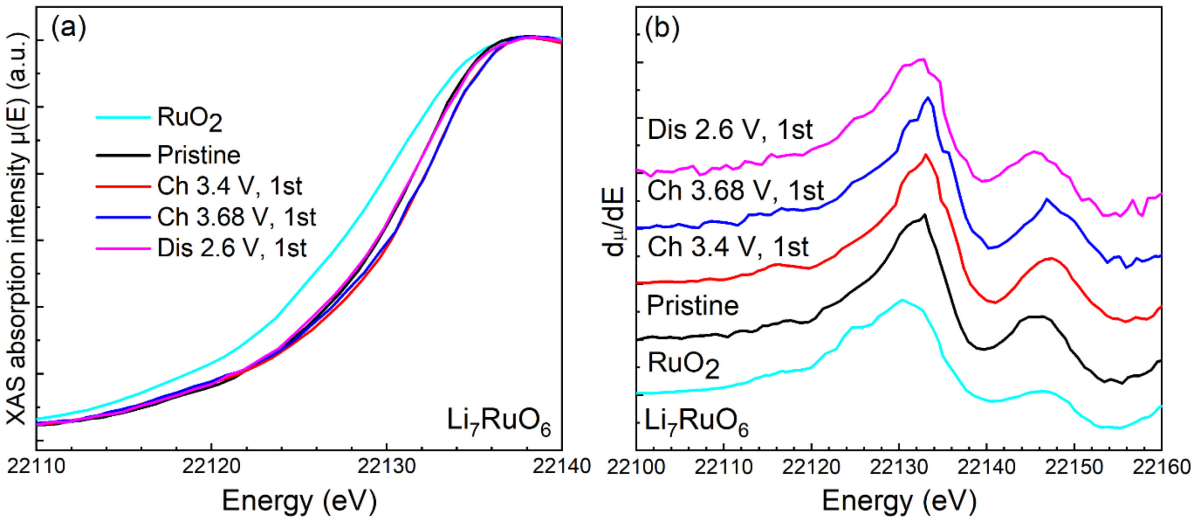

Figure 4. (a) *Ex situ* Ru K-edge XANES spectra of Li_7RuO_6 at different states of charge in the voltage window of 2.6-3.68 V as well as RuO_2 reference, and (b) the corresponding first derivative.

To explore the variation of the electronic structure of O during the same redox reactions, *ex situ* O K-edge XAS measurements were carried out. Signals arise from dipole-allowed transitions from core O *1s* orbitals to unoccupied O *2p* states. The pre-edge region, at ≤ 535 eV, represents the unoccupied states resulting from O *2p* orbitals hybridized with Ru *4d* orbitals, and the broad band above 535 eV corresponds to the excitation from localized O *1s* orbital to empty states of O *2p* orbitals mixed with Ru *5s* and *5p* orbitals, followed by higher states and multiple scattering

events of the ejected electrons. The position of the pre-edge peaks is affected by the relative change in O *1s* and 2*p* levels energy depending on the effective nuclear charge, Z_{eff} of O, the ligand field splitting, and the strength of Ru-O overlap. Their intensity reflects both the number of unoccupied hybridized states and the contribution of O to their wavefunction. The position of the rising edge in the broad band can be deduced from the 1st derivative of the XAS spectrum and provides insight into the binding energy of the O 1*s* level. XAS was measured simultaneously under both TEY and TFY modes, with probing depths around 10 and 100 nm into the electrode, respectively. The TEY spectra showed a prominent peak at 533.8 eV (Figure S8), which has been attributed to π^* (C=O) orbitals in carbonated-related species (like Li_2CO_3) present on the sample surface. Thus, analysis mainly focused on TFY spectra, where the bulk is dominant (Figure 5a). Since spectral intensities in TFY are distorted by the self-absorption, only relative trends will be established.

The O K-edge XAS spectrum of Li_7RuO_6 displayed distinct pre-edge features centered at 528.4, 530.5, and 532 eV, respectively (Figure 5a). In accordance with ligand field theory, the sharp peak at 528.4 eV is assigned to unoccupied orbitals of O 2*p*-Ru 4*d* states with a π interaction, whereas the intense signal at 532 eV and a shoulder at around 530.5 eV is assigned to unoccupied orbitals of O 2*p*-Ru 4*d* states with a σ interaction. The lower relative intensity of the signals associated with σ compared to π interactions reflects the d^3 configuration of Ru(V), and is reminiscent of previous observations of Li_3RuO_4.[36] The O K-edge XAS was computed using non-spin polarized ground state calculations (Figure 6a). The computed spectrum reproduced the position of three main peaks in the spectra at 528.4 eV ("α"), 532 eV ("β") and 534.8 eV ("γ"), yet the relative intensities showed discrepancies. The shoulder around 530.5 eV was not captured by simulations without spin polarization. When such polarization was introduced, the resulting simulated XAS displayed more complex features in the pre-edge (Figure 6a), which, in turn, depended on the

magnetic ground state of Ru reached in the converged calculations. Some of these features could plausibly be associated with the experimental shoulder, suggesting that further details of the magnetic ground state are needed to fully explain the spectra. The peak around 535 eV was not affected by the magnetic configuration of the Ru 4*d* states, so it was correspondingly assigned to higher O 2*p*-Ru 5*s,p* hybridized states, in agreement with previous literature.[60] Projection of XAS on individual O atoms (Figure S9) showed that signal splitting is dominated by the ligand field, rather than a shift of individual oxygen spectrum with respect to each other as observed in Li_3IrO_4[25].

Upon oxidation to 3.4 V, the peak at lowest energy redshifted by 0.3 eV concurrent with a noticeable intensity reduction relative to the pristine state (Figures 5a). A new shoulder feature emerged at around 527.2 eV, indicating a formation of new unoccupied states, and raising the overall intensity below 530 eV (Figure 5b). The peak at 532 eV underwent a remarkable intensity rise, although its position was stable (Figures 5a and S10). The corresponding shoulder initially located at 530.5 eV moved to 531.1 eV with increased intensity. No obvious trend could be extracted from the analysis of the inflection at the absorption edge, above 535 eV (Figure S11). The changes in the peak position and intensity at the pre-edge part reflected the notable changes taking place in the hybridization of the O 2*p*-Ru 4*d* orbitals.

Contrary to the absence of visible changes at the Ru K-edge and in the XRD, further oxidation affected the O K-edge XAS (Figures 5a). First, further increases in relative intensity were observed at around 528.1 eV, including its shoulder at 527.2 eV, and, to a lesser extent, between 530 and 532 eV (Figures 5b and 5d). There was no significant shift in the centroids of the pre-edge, with the exception of the shoulder at 530 eV. Lastly, there was a clear decrease in the intensity of the feature at 535 eV (Figures 5a and 5c), yet no clear shifts of the inflection point were noticed at the

absorption edge (Figure S11). Reduction back to 2.6 V restored the spectral features largely to the pristine state, implying a reversible process, consistent with the other characterization results.

The simulations of XAS (Figures 6b and 6c and S12) of two theoretical states, Li_6RuO_6 and Li_5RuO_6, using structures predicted from the convergence to the most stable arrangements at each composition, largely reproduced the trends upon delithiation of Li_7RuO_6. It is worth noting that the converged arrangements predicted a preservation of the octahedral coordination around Ru, consistent with the absence of a pre-edge feature in the XAS and the EXAF analysis, and contrary to other reports of formation of Ru(VI) demanding a tetrahedral environment.[42] The depopulation of O 2*p*-Ru 4*d* states led to an increase of the crystal field splitting concomitant with the increase in intensity below 530 eV (Figure 5b). The oxygen atoms in proximity of lithium that are removed are preferentially oxidized, as reflected by the Bader charge analysis and the associated shortening of the Ru-O bonds due to the increase in covalency **(**Table 2**)**. The variations in the Ru-O bond distances within a single RuO_6 unit cause subtle relative shifts of the spectra from individual oxygen atoms (the colour code in Figures 6b and 6c is explained in Figure S12). As with the pristine phase, the peak shapes originate from interaction of individual oxygen atoms with the metal *d* orbitals. Further, they were found to be sensitive to the magnetic ground state obtained in the converged calculations, and it could account for the comparably more complex lineshapes observed in the experimental spectra. Various distributions of lithium vacancies were considered, but they did only affect the spectral features above the pre-edge (i.e., around 535 eV and higher).

When Li_5RuO_6 is reached, the peak around 535 eV is no longer present in the calculated XAS. In contrast to Li_7RuO_6 and Li_6RuO_6 where lithium sits in tetrahedral and octahedral environments, all Li atoms lie in octahedral positions in Li_5RuO_6 structure. As a result, we propose that the peak at 535 eV is due to polarization effects of the oxygen electron cloud due to Li site occupancies.

This peak decreases in the experimental spectra, suggesting that Li removal compensated by states other than O 2*p*-Ru 4*d* is possible. However, it never vanishes completely, probably because the experimental composition where the spectra was collected corresponded to $Li_{5.7}RuO_6$, assuming 100% faradaic efficiency, rather than Li_5RuO_6.

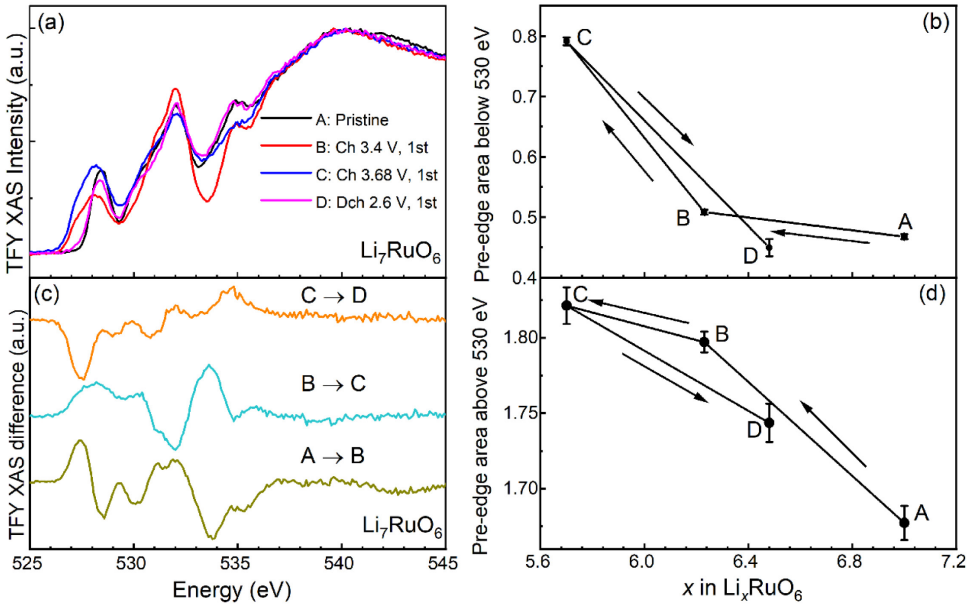

Figure 5. (a) *Ex situ* O K-edge XAS spectra of Li_7RuO_6 at different states of charge in the voltage window of 2.6-3.68 V measured in TFY mode. (d) Differential XAS spectra between states of charge indicated. Variations in relative pre-edge intensity as a function of x in Li_xRuO_6 integrated (b) below and (c) above 530 eV.

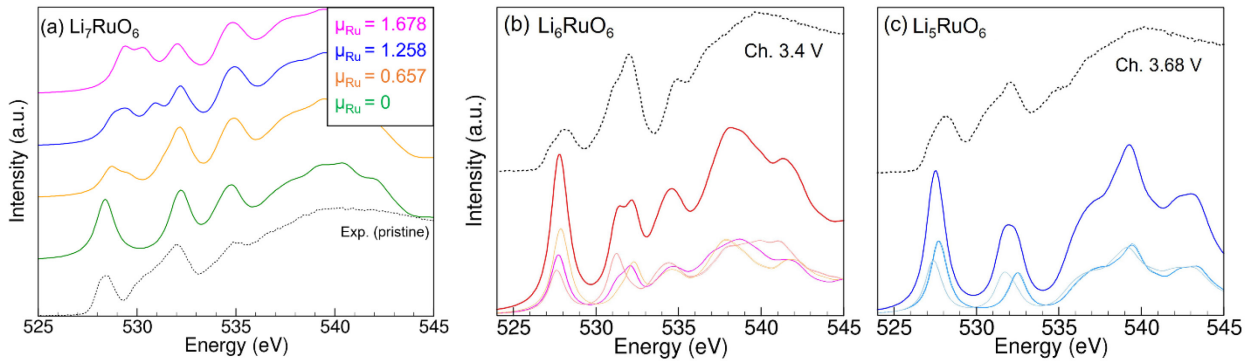

Figure 6. (a) Comparison of observed and calculated O K-edge XAS for Li_7RuO_6 ($P\bar{1}$). The

theoretical spectra were calculated in the absence/presence of spin polarization of Ru ground state. The calculation with the absence of ground state spin polarization of Ru well matches the observed one. In addition, the peak "γ" is not affected by the spin polarization of Ru and should not be associated with hybridized Ru 4*d*-O 2*p* states. Panels (b) and (c) show the same comparison for Li_6RuO_6 and Li_5RuO_6, respectively, with projected XAS included. The simulated spectra are obtained from ground state structures emerging from non-spin-polarized calculations (corresponding spectra including spin-polarization are in Figure S12).

Table 2. Bader net population for Ru and O at different delithiation stages. Initially, the O atoms are equivalent, and small variations in the net population come from small differences in Ru-O bond lengths. Removal of Li leads to removing electrons from Ru-O covalent bonds and the atoms that are oxidized first are the ones in the proximity of Li vacancy. Differentiation of Ru-O bonds becomes more pronounced at lower lithium content (Li_6RuO_6 and Li_5RuO_6), where depletion of charge is most pronounced in O that displays the shotest distance with Ru.

	Li_5RuO_6		Li_6RuO_6		Li_7RuO_6	
	Net population	Ru-O (A)	Net population	Ru-O (A)	Net population	Ru-O (A)
Ru	-1.9703	-	-1.9088	-	-1.7869	
O1	0.9737	1.844	1.1690	1.919	1.2475	1.954
O2	0.9712	1.844	1.1690	1.919	1.2957	2.000
O3	1.0801	1.905	1.2409	1.984	1.2455	1.970
O4	1.0798	1.905	1.2411	1.984	1.3361	2.042
O5	1.0816	1.905	1.0800	1.880	1.2641	1.974
O6	1.0814	1.905	1.0801	1.880	1.2549	1.968

3.3 Voltage cutoff window of 1.6-2.6 V

Upon initial reduction to 1.5 V, a long plateau was observed at around 2.2 eV versus Li^+/Li in the electrochemical profile of the Li_7RuO_6 electrode (Figure 7), accumulating a capacity equivalent to approximately 1 mol Li per mol compound, reaching Li_8RuO_6. The reverse oxidation occurred at ~2.23 V, concomitant with the extraction of 1 mol Li, reflecting an exceedingly small voltage hysteresis. The profiles of subsequent cycling remained with a slight loss in the capacity, indicating a high reversibility of the redox process associated with Li^+ insertion/removal.

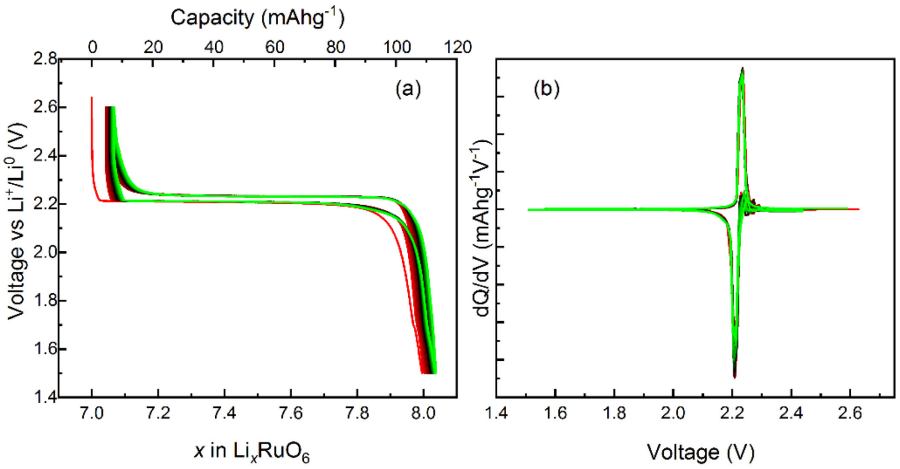

Figure 7. (a) Charge-composition profiles of Li_7RuO_6 between 1.5 and 2.6 V and (b) the corresponding dQ/dV plots.

The *ex situ* SXRD pattern after reduction to 1.5 V (Figure 8) could be indexed with a $R\bar{3}$ space group, corresponding to a transition to a trigonal structure. Rietveld refinement was carried out to extract detailed structural information (Figure 9 and Table 3). The results demonstrated that the previously vacant sites in Li_7RuO_6 were fully filled by intercalated Li. The increase in symmetry led to only two unique sites for Li, with tetrahedral symmetry in the Li layers and octahedral symmetry in the metal layers, as demonstrated by the structure in Figure 8. The peak positions and intensity returned to the pristine state after the subsequent oxidation (Figure 8a), reflecting a highly

reversible cycling process. Again, similar to the 2.5-3.68 V cycling voltage window, *ex situ* SXRD data collected after the 2nd discharge-charge cycle (Figure 8b) further substantiated the high chemical reversibility associated with Li insertion and removal.

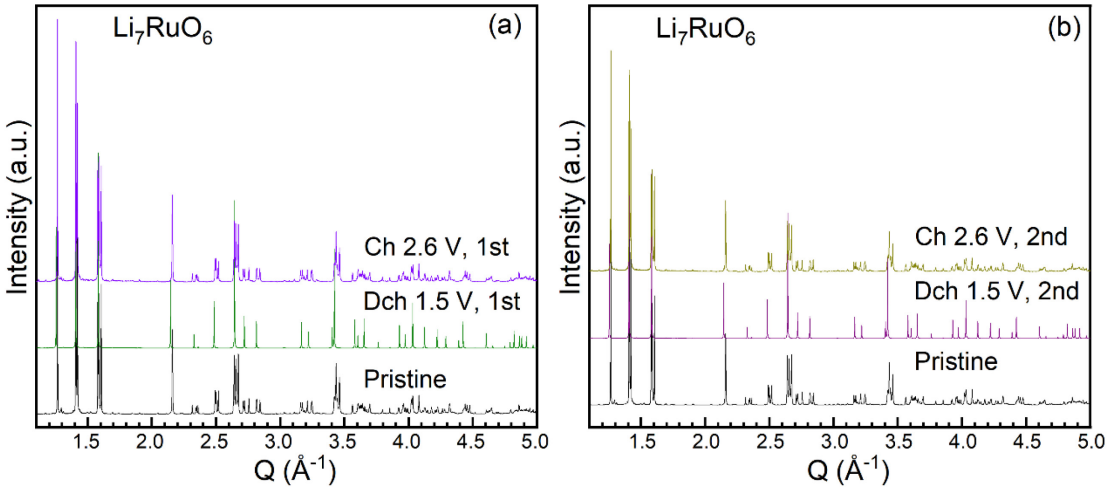

Figure 8. *Ex situ* SXRD patterns of Li_7RuO_6 upon (a) the first and (b) the second cycling between 1.5 V and 2.6 V.

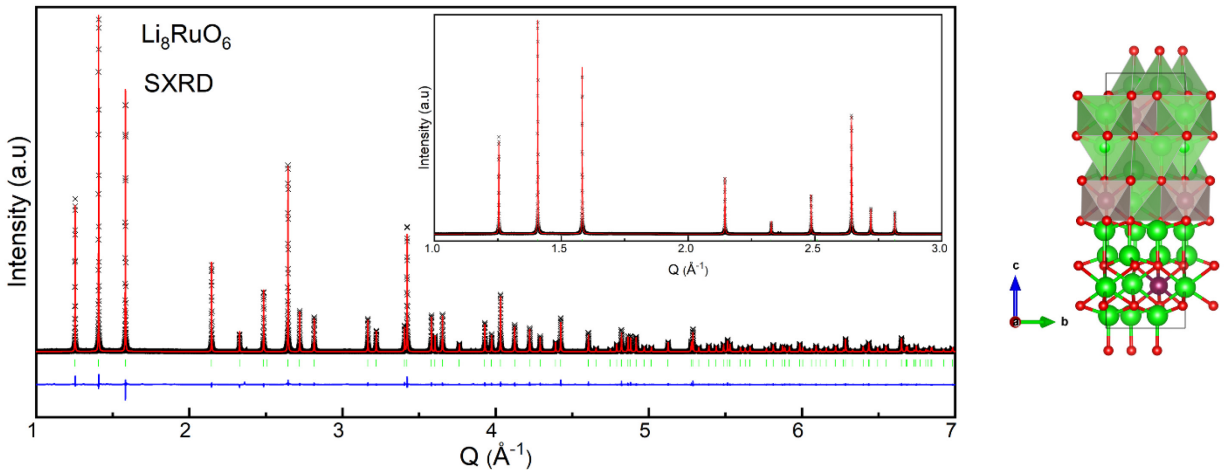

Figure 9. Rietveld refinement of SXRD patters of Li_7RuO_6 after reduction to 1.5 V. The black crosses, and red solid line correspond to experimental and calculated patterns, respectively. The blue solid line represents different patterns between experimental and calculated ones. Vertical

green bars dictate Bragg reflections. Inset is the zoom-in part of X-ray diffraction with the range of 1-3 $Å^{-1}$ to illustrate the absence of peak splitting found in the pristine state, due to the increased symmetry. The right panel represents the corresponding structure. O, Ru, and Li are in red, blue, and green, respectively. Both polyhedral and ball-and-stick depictions are presented to maximize the visibility of the structural features.

Table 3. Crystallographic parameters and reliability factors extracted from the combined Rietveld refinement of SXRD for Li_7RuO_6 after reduction to 1.5 V.

Li_8RuO_6 Space group: $R\bar{3}$; a = 5.399156(7) Å; b = 5.399156(7) Å; c = 15.031874(15) Å; α = 90°; β = 90°; γ = 120°; V = 379.4857(7) $Å^3$						
Atom	Wyckoff position	x	y	z	Uiso ($Å^2$)	Occupancy
Ru1	3a	1/3	22/3	1/6	0.00149(5)	1.000
O1	18f	0.02106(16)	0.65590(17)	0.24534(5)	0.0042(4)	1.000
Li1	18f	0.6861(5)	0.0356(5)	0.04953(14)	0.0072(11)	1.000
Li2	6c	2/3	1/3	0.17349(17)	0.0140(9)	1.000
R_{WP} = 10.094%; R_F = 2.440%; R_B = 5.780%; χ^2 = 1.980.						

The initial Li intercalation brought about a large low-energy shift of the Ru K-edge absorption by 2.2 eV (Figure 10a), in close proximity to the position of RuO_2, clearly indicating Ru(V)/Ru(IV) reduction. The subsequent oxidation reaction led to the recovery of the absorption edge to the position of the pristine state, clearly illustrating a reversible redox change. Changes in the EXAFS oscillations were also reversible, with the Ru-O distance increasing to 2.03 Å and reverting back to 1.96 Å, while preserving a coordination number around 6 (Figure S6 and Table S2). The most visible change upon Li intercalation on the *ex situ* O K-edge XAS (Figure 10b) was the shift of the peak at lowest energy from 528.4 eV to 528.7 eV, concurrent to a noticeable decrease in its intensity. The other pre-edge features underwent little variation in the position and only a small reduction in the normalized integrated intensity (Figures 10b). Subsequent oxidation to 2.6 V

restored the spectrum to the pristine state (Figure 10b). No obvious trends were noticed in the inflection point at the absorption edge, above 535 eV, throughout the process (Figure S13). Overall, the variation in the XAS spectra reflects a highly reversible intercalation reaction in the voltage window of 1.5-2.6 V. The computed O K-edge XAS and the corresponding projected density of states for Li_8RuO_6 (Figures 10c-e) shows that the decrease in the first peak is due to the filling of the antibonding O 2*p*-Ru 4*d* orbitals states with a π symmetry (t_{2g} in an ideal O_h field). Although spin-polarized calculations with constrained magnetic structures can lead to subtle differences between all spectra, the closest match between measured and computed spectra was achieved when the magnetic ground states were considered (Figure S14).

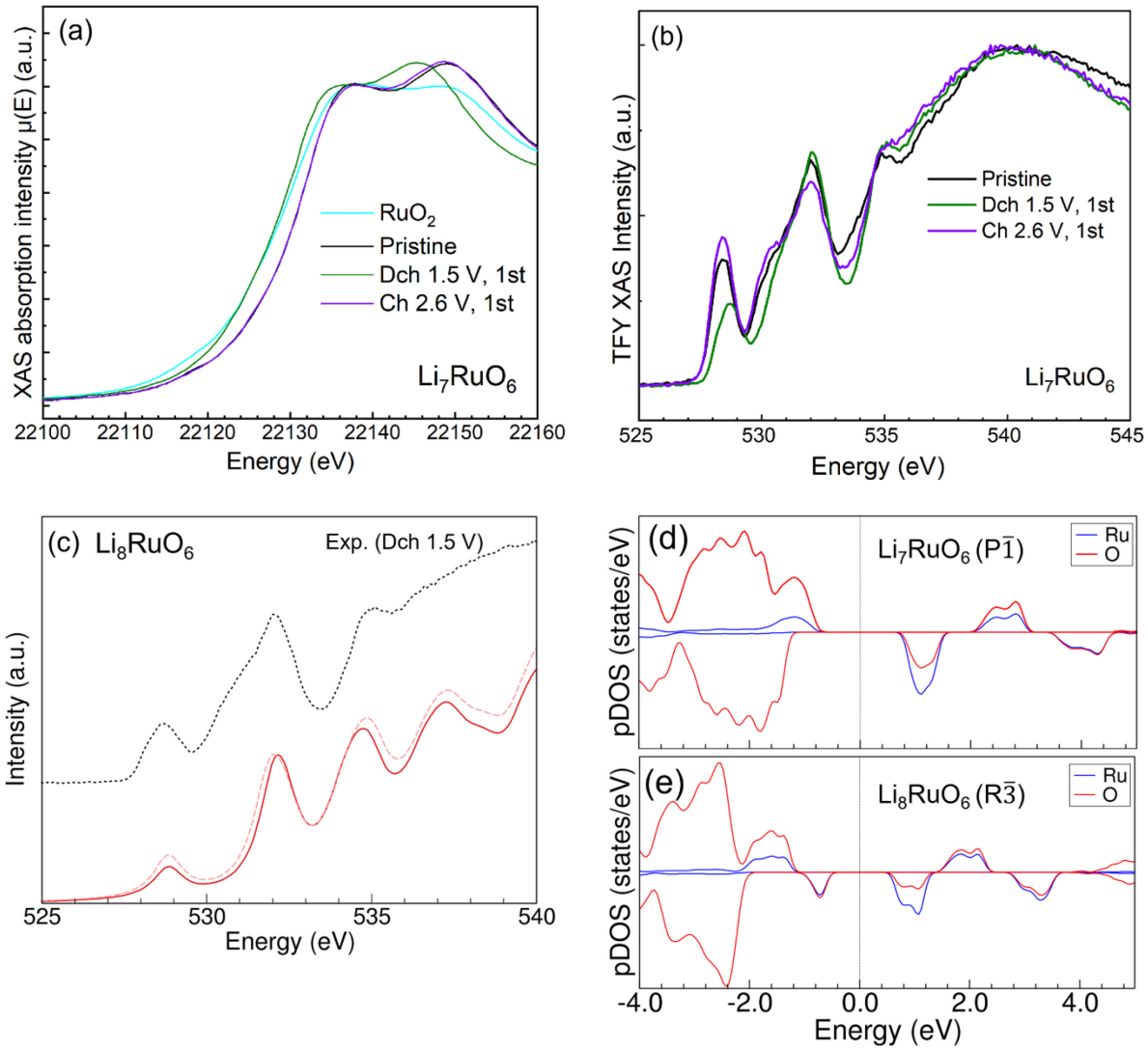

Figure 10. (a) Overlaid e*x situ* Ru K-edge XANES spectra of Li_7RuO_6 at different states of charge in the 1.5-2.6 voltage window as well as the reference RuO_2. (b) *Ex situ* O K-edge XAS spectra of Li_7RuO_6 at different states of charge in the voltage window of 1.5-2.6 V measured under TFY mode. (c) Experimental and calculated O K-edge for the reduced Li_8RuO_6 structure belonging to $R\bar{3}$ space group. The structure taken directly from the XRD measurements (solid line) and the structure relaxed afterwods within DFT (dashed line) are compared. The XAS is obtained based on non-spin-polarized ground state calculations and shows good agreement with experimental spectra. The projected density of states (pDOS) for (d) Li_7RuO_6 and (e) Li_8RuO_6 clearly shows

reduction of peak corresponding to *Ru(d_{t2g})-O(p)* states. The pDOS was obtained using Quantum Espresso with NCPP and within GGA+U=4eV.

4. Conclusion

Li_7RuO_6 undergoes Li intercalation between 1.5 and 2.6 V to form Li_8RuO_6 through a classical topotactic process with the charge compensation through a formal change in oxidation state of Ru from V to IV, as a proxy for states with Ru and O covalent hybridization. The oxide also displays reversible anodic activity in the window of 2.6-3.4 V. Analysis of the electronic structure reveals that $Li_{7-x}RuO_6$ initially undergoes formal oxidation of Ru(V) to Ru(VI), in staggering contrast with $Li_{3-x}RuO_4$ and $Li_{2-x}RuO_3$, where unconventional processes centered on O have been reported beyond Ru(V). Furthermore, both computational and experimental results indicate that formation of Ru(VI) can be achieved within an octahedral environment, providing a unique example of such an unusual oxidation state without requiring tetrahedral coordination, made in mild conditions. While this activity was less efficient than at low potential overall, subsequent reduction was accompanied by a complete return to the initial chemical state, without any hysteresis in chemical pathway. The results showcase the diversity of redox chemistry even within a constrained chemical space such as lithium ruthenium oxides, suggesting the existence of refined control knobs to leverage such redox for important functional applications, such as battery electrodes.

ASSOCIATED CONTENT

Supporting Information

The Supporting Information is available free of charge on the ACS Publications website at DOI:

Figure S1-S14 and Table S1-S2. Alternative plots of the data in the article; additional analysis of the XAS data, including Ru K-edge EXAFS; supplementary computations of O K-edge XAS data; supplementary XRD data.

Acknowledgements

This material is based upon work supported by the National Science Foundation under Grant No. DMR-1809372. This research used resources of the Advanced Photon Source, a U.S. Department of Energy (DOE) Office of Science User Facility operated for the DOE Office of Science by Argonne National Laboratory under Contract No. DE-AC02-06CH11357.

References

1. Noorden, R. V., The rechargeable revolution: A better battery. *Nature* **2014,** 507, (7490), 26-28.

2. Whittingham, M. S., Ultimate Limits to Intercalation Reactions for Lithium Batteries. *Chem. Rev.* **2014,** 114, (23), 11414-11443.

3. Dunn, B.; Kamath, H.; Tarascon, J.-M., Electrical Energy Storage for the Grid: A Battery of Choices. *Science* **2011,** 334, (6058), 928-935.

4. Zubi, G.; Dufo-López, R.; Carvalho, M.; Pasaoglu, G., The lithium-ion battery: State of the art and future perspectives. *Renew. Sust. Energ. Rev.* **2018,** 89, 292-308.

5. Trahey, L.; Brushett, F. R.; Balsara, N. P.; Ceder, G.; Cheng, L.; Chiang, Y.-M.; Hahn, N. T.; Ingram, B. J.; Minteer, S. D.; Moore, J. S.; Mueller, K. T.; Nazar, L. F.; Persson, K. A.; Siegel, D. J.; Xu, K.; Zavadil, K. R.; Srinivasan, V.; Crabtree, G. W., Energy storage emerging: A

perspective from the Joint Center for Energy Storage Research. *Proc. Natl. Acad. Sci.* **2020,** 117, (23), 12550-12557.

6. Manthiram, A., A reflection on lithium-ion battery cathode chemistry. *Nat. Commun.* **2020,** 11, (1), 1550.

7. Li, M.; Liu, T.; Bi, X.; Chen, Z.; Amine, K.; Zhong, C.; Lu, J., Cationic and anionic redox in lithium-ion based batteries. *Chem. Soc. Rev.* **2020,** 49, (6), 1688-1705.

8. Mizushima, K.; Jones, P. C.; Wiseman, P. J.; Goodenough, J. B., Li_xCoO_2 ($0<x<1$): A new cathode material for batteries of high energy density. *Mater. Res. Bull.* **1980,** 15, (6), 783-789.

9. Reimers, J. N., Electrochemical and In Situ X-Ray Diffraction Studies of Lithium Intercalation in Li_xCoO_2. *J. Electrochem. Soc.* **1992,** 139, (8), 2091.

10. Amatucci, G. G.; Tarascon, J. M.; Klein, L. C., CoO_2, The End Member of the Li_xCoO_2 Solid Solution. *J. Electrochem. Soc.* **1996,** 143, (3), 1114.

11. Carlier, D.; Van der Ven, A.; Delmas, C.; Ceder, G., First-Principles Investigation of Phase Stability in the O2-$LiCoO_2$ System. *Chem. Mater.* **2003,** 15, (13), 2651-2660.

12. Zhang, J.-N.; Li, Q.; Ouyang, C.; Yu, X.; Ge, M.; Huang, X.; Hu, E.; Ma, C.; Li, S.; Xiao, R.; Yang, W.; Chu, Y.; Liu, Y.; Yu, H.; Yang, X.-Q.; Huang, X.; Chen, L.; Li, H., Trace doping of multiple elements enables stable battery cycling of $LiCoO_2$ at 4.6 V. *Nat. Energy* **2019,** 4, (7), 594-603.

13. Lee, J.; Kitchaev, D. A.; Kwon, D.-H.; Lee, C.-W.; Papp, J. K.; Liu, Y.-S.; Lun, Z.; Clément, R. J.; Shi, T.; McCloskey, B. D.; Guo, J.; Balasubramanian, M.; Ceder, G., Reversible Mn^{2+}/Mn^{4+} double redox in lithium-excess cathode materials. *Nature* **2018,** 556, (7700), 185-190.

14. Seo, D. H.; Lee, J.; Urban, A.; Malik, R.; Kang, S.; Ceder, G., The structural and chemical origin of the oxygen redox activity in layered and cation-disordered Li-excess cathode materials. *Nat. Chem.* **2016,** 8, (7), 692-7.

15. Sathiya, M.; Rousse, G.; Ramesha, K.; Laisa, C. P.; Vezin, H.; Sougrati, M. T.; Doublet, M. L.; Foix, D.; Gonbeau, D.; Walker, W.; Prakash, A. S.; Ben Hassine, M.; Dupont, L.; Tarascon, J. M., Reversible anionic redox chemistry in high-capacity layered-oxide electrodes. *Nat. Mater.* **2013,** 12, (9), 827-35.

16. Gent, W. E.; Lim, K.; Liang, Y.; Li, Q.; Barnes, T.; Ahn, S. J.; Stone, K. H.; McIntire, M.; Hong, J.; Song, J. H.; Li, Y.; Mehta, A.; Ermon, S.; Tyliszczak, T.; Kilcoyne, D.; Vine, D.; Park, J. H.; Doo, S. K.; Toney, M. F.; Yang, W.; Prendergast, D.; Chueh, W. C., Coupling between oxygen redox and cation migration explains unusual electrochemistry in lithium-rich layered oxides. *Nat. Commun.* **2017,** 8, (1), 2091.

17. Pearce, P. E.; Perez, A. J.; Rousse, G.; Saubanère, M.; Batuk, D.; Foix, D.; McCalla, E.; Abakumov, A. M.; Van Tendeloo, G.; Doublet, M.-L.; Tarascon, J.-M., Evidence for anionic redox activity in a tridimensional-ordered Li-rich positive electrode β-Li_2IrO_3. *Nat. Mater.* **2017,** 16, (5), 580-586.

18. Lee, G.-H.; Wu, J.; Kim, D.; Cho, K.; Cho, M.; Yang, W.; Kang, Y.-M., Reversible Anionic Redox Activities in Conventional $LiNi_{1/3}Co_{1/3}Mn_{1/3}O_2$ Cathodes. *Angew. Chem. Int. Ed.* **2020,** 59, (22), 8681-8688.

19. Yabuuchi, N.; Takeuchi, M.; Nakayama, M.; Shiiba, H.; Ogawa, M.; Nakayama, K.; Ohta, T.; Endo, D.; Ozaki, T.; Inamasu, T.; Sato, K.; Komaba, S., High-capacity electrode materials for rechargeable lithium batteries: Li_3NbO_4-based system with cation-disordered rocksalt structure. *Proc. Natl. Acad. Sci.* **2015,** 112, (25), 7650-7655.

20. Jacquet, Q.; Iadecola, A.; Saubanère, M.; Li, H.; Berg, E. J.; Rousse, G.; Cabana, J.; Doublet, M.-L.; Tarascon, J.-M., Charge Transfer Band Gap as an Indicator of Hysteresis in Li-Disordered Rock Salt Cathodes for Li-Ion Batteries. *J. Am. Chem. Soc.* **2019,** 141, (29), 11452-11464.

21. Yue, Y.; Ha, Y.; Huang, T.-Y.; Li, N.; Li, L.; Li, Q.; Feng, J.; Wang, C.; McCloskey, B. D.; Yang, W.; Tong, W., Interplay between Cation and Anion Redox in Ni-Based Disordered Rocksalt Cathodes. *ACS Nano* **2021,** 15, (8), 13360-13369.

22. House, R. A.; Maitra, U.; Pérez-Osorio, M. A.; Lozano, J. G.; Jin, L.; Somerville, J. W.; Duda, L. C.; Nag, A.; Walters, A.; Zhou, K.-J.; Roberts, M. R.; Bruce, P. G., Superstructure control of first-cycle voltage hysteresis in oxygen-redox cathodes. *Nature* **2020,** 577, (7791), 502-508.

23. Jia, M.; Li, H.; Qiao, Y.; Wang, L.; Cao, X.; Cabana, J.; Zhou, H., Elucidating Anionic Redox Chemistry in P3 Layered Cathode for Na-Ion Batteries. *ACS Appl. Mater. Interfaces* **2020,** 12, (34), 38249-38255.

24. Perez, A. J.; Jacquet, Q.; Batuk, D.; Iadecola, A.; Saubanère, M.; Rousse, G.; Larcher, D.; Vezin, H.; Doublet, M.-L.; Tarascon, J.-M., Approaching the limits of cationic and anionic electrochemical activity with the Li-rich layered rocksalt Li_3IrO_4. *Nat. Energy* **2017,** 2, (12), 954-962.

25. Li, H.; Perez, A. J.; Taudul, B.; Boyko, T. D.; Freeland, J. W.; Doublet, M.-L.; Tarascon, J.-M.; Cabana, J., Elucidation of Active Oxygen Sites upon Delithiation of Li_3IrO_4. *ACS Energy Lett.* **2021,** 6, (1), 140-147.

26. Yoon, W.-S.; Kim, K.-B.; Kim, M.-G.; Lee, M.-K.; Shin, H.-J.; Lee, J.-M.; Lee, J.-S.; Yo, C.-H., Oxygen Contribution on Li-Ion Intercalation−Deintercalation in $LiCoO_2$ Investigated by O

K-Edge and Co L-Edge X-ray Absorption Spectroscopy. *J. Phys. Chem. B* **2002,** 106, (10), 2526-2532.

27. Lebens-Higgins, Z. W.; Faenza, N. V.; Radin, M. D.; Liu, H.; Sallis, S.; Rana, J.; Vinckeviciute, J.; Reeves, P. J.; Zuba, M. J.; Badway, F.; Pereira, N.; Chapman, K. W.; Lee, T.-L.; Wu, T.; Grey, C. P.; Melot, B. C.; Van Der Ven, A.; Amatucci, G. G.; Yang, W.; Piper, L. F. J., Revisiting the charge compensation mechanisms in $LiNi_{0.8}Co_{0.2-y}Al_yO_2$ systems. *Mater. Horiz.* **2019,** 6, (10), 2112-2123.

28. Oishi, M.; Yamanaka, K.; Watanabe, I.; Shimoda, K.; Matsunaga, T.; Arai, H.; Ukyo, Y.; Uchimoto, Y.; Ogumi, Z.; Ohta, T., Direct observation of reversible oxygen anion redox reaction in Li-rich manganese oxide, Li_2MnO_3, studied by soft X-ray absorption spectroscopy. *J. Mater. Chem. A* **2016,** 4, (23), 9293-9302.

29. Ramakrishnan, S.; Park, B.; Wu, J.; Yang, W.; McCloskey, B. D., Extended Interfacial Stability through Simple Acid Rinsing in a Li-Rich Oxide Cathode Material. *J. Am. Chem. Soc.* **2020,** 142, (18), 8522-8531.

30. Rana, J.; Papp, J. K.; Lebens-Higgins, Z.; Zuba, M.; Kaufman, L. A.; Goel, A.; Schmuch, R.; Winter, M.; Whittingham, M. S.; Yang, W.; McCloskey, B. D.; Piper, L. F. J., Quantifying the Capacity Contributions during Activation of Li_2MnO_3. *ACS Energy Lett.* **2020,** 5, (2), 634-641.

31. Radin, M. D.; Vinckeviciute, J.; Seshadri, R.; Van der Ven, A., Manganese oxidation as the origin of the anomalous capacity of Mn-containing Li-excess cathode materials. *Nat. Energy* **2019,** 4, (8), 639-646.

32. Sathiya, M.; Ramesha, K.; Rousse, G.; Foix, D.; Gonbeau, D.; Prakash, A. S.; Doublet, M. L.; Hemalatha, K.; Tarascon, J. M., High Performance $Li_2Ru_{1-y}Mn_yO_3$ ($0.2 \leq y \leq 0.8$) Cathode

Materials for Rechargeable Lithium-Ion Batteries: Their Understanding. *Chem. Mater.* **2013,** 25, (7), 1121-1131.

33. Sathiya, M.; Abakumov, A. M.; Foix, D.; Rousse, G.; Ramesha, K.; Saubanere, M.; Doublet, M. L.; Vezin, H.; Laisa, C. P.; Prakash, A. S.; Gonbeau, D.; VanTendeloo, G.; Tarascon, J. M., Origin of voltage decay in high-capacity layered oxide electrodes. *Nat. Mater.* **2015,** 14, (2), 230-8.

34. Sarkar, S.; Mahale, P.; Mitra, S., Lithium Rich Composition of Li_2RuO_3 and $Li_2Ru_{1-x}Ir_xO_3$ Layered Materials as Li-Ion Battery Cathode. *J. Electrochem. Soc.* **2014,** 161, (6), A934-A942.

35. Jacquet, Q.; Iadecola, A.; Saubanère, M.; Lemarquis, L.; Berg, E. J.; Alves Dalla Corte, D.; Rousse, G.; Doublet, M.-L.; Tarascon, J.-M., Competition between Metal Dissolution and Gas Release in Li-Rich $Li_3Ru_yIr_{1-y}O_4$ Model Compounds Showing Anionic Redox. *Chem. Mater.* **2018,** 30, (21), 7682-7690.

36. Li, H.; Ramakrishnan, S.; Freeland, J. W.; McCloskey, B. D.; Cabana, J., Definition of Redox Centers in Reactions of Lithium Intercalation in Li_3RuO_4 Polymorphs. *J. Am. Chem. Soc.* **2020,** 142, (18), 8160-8173.

37. Zhuo, Z.; Dai, K.; Wu, J.; Zhang, L.; Tamura, N.; Chuang, Y.-d.; Feng, J.; Guo, J.; Shen, Z.-x.; Liu, G.; Pan, F.; Yang, W., Distinct Oxygen Redox Activities in Li_2MO_3 (M = Mn, Ru, Ir). *ACS Energy Lett.* **2021,** 6, (10), 3417-3424.

38. Assat, G.; Iadecola, A.; Delacourt, C.; Dedryvère, R.; Tarascon, J.-M., Decoupling Cationic–Anionic Redox Processes in a Model Li-Rich Cathode via Operando X-ray Absorption Spectroscopy. *Chem. Mater.* **2017,** 29, (22), 9714-9724.

39. Yu, Y.; Karayaylali, P.; Nowak, S. H.; Giordano, L.; Gauthier, M.; Hong, W.; Kou, R.; Li, Q.; Vinson, J.; Kroll, T.; Sokaras, D.; Sun, C.-J.; Charles, N.; Maglia, F.; Jung, R.; Shao-Horn, Y.,

Revealing Electronic Signatures of Lattice Oxygen Redox in Lithium Ruthenates and Implications for High-Energy Li-Ion Battery Material Designs. *Chem. Mater.* **2019,** 31, (19), 7864-7876.

40. Xie, Y.; Saubanère, M.; Doublet, M. L., Requirements for reversible extra-capacity in Li-rich layered oxides for Li-ion batteries. *Energy Environ. Sci.* **2017,** 10, (1), 266-274.

41. Jacquet, Q.; Perez, A.; Batuk, D.; Van Tendeloo, G.; Rousse, G.; Tarascon, J.-M., The $Li_3Ru_yNb_{1-y}O_4$ ($0 \leq y \leq 1$) System: Structural Diversity and Li Insertion and Extraction Capabilities. *Chem. Mater.* **2017,** 29, (12), 5331-5343.

42. Otoyama, M.; Jacquet, Q.; Iadecola, A.; Saubanère, M.; Rousse, G.; Tarascon, J.-M., Synthesis and Electrochemical Activity of Some Na(Li)-Rich Ruthenium Oxides with the Feasibility to Stabilize Ru^{6+}. *Adv. Energy Mater.* **2019,** 9, (15), 1803674.

43. Mühle, C.; Karpov, A.; Verhoeven, A.; Jansen, M., Crystal Structures, Dimorphism and Lithium Mobility of Li_7MO_6 (M = Bi, Ru, Os). *Z. Anorg. Allg. Chem.* **2005,** 631, (12), 2321-2327.

44. Nakajima, K.; Sato, H.; Fukui, T.; Iwaki, M.; Narumi, Y.; Kindo, K.; Itoh, Y.; Michioka, C.; Yoshimura, K., Li_7RuO_6: As a 4d Heisenberg Frustrated Magnet. *J. Phys. Soc. Japan* **2010,** 79, (6), 064705.

45. Toby, B. H.; Von Dreele, R. B., GSAS-II: the genesis of a modern open-source all purpose crystallography software package. *J. Appl. Crystallogr.* **2013,** 46, (2), 544-549.

46. Ravel, B.; Newville, M., ATHENA, ARTEMIS, HEPHAESTUS: data analysis for X-ray absorption spectroscopy using IFEFFIT. *J. Synchrotron Rad.* **2005,** 12, (4), 537-541.

47. Kresse, G.; Furthmüller, J., Efficient iterative schemes for ab initio total-energy calculations using a plane-wave basis set. *Phys. Rev. B* **1996,** 54, (16), 11169-11186.

48. Kresse, G.; Joubert, D., From ultrasoft pseudopotentials to the projector augmented-wave method. *Phys. Rev. B* **1999,** 59, (3), 1758-1775.

49. Biffin, A.; Johnson, R. D.; Choi, S.; Freund, F.; Manni, S.; Bombardi, A.; Manuel, P.; Gegenwart, P.; Coldea, R., Unconventional magnetic order on the hyperhoneycomb Kitaev lattice in Li_2IrO_3: Full solution via magnetic resonant x-ray diffraction. *Phys. Rev. B* **2014,** 90, (20), 205116.

50. Perdew, J. P.; Burke, K.; Ernzerhof, M., Generalized Gradient Approximation Made Simple. *Phys. Rev. Lett.* **1996,** 77, (18), 3865-3868.

51. Dudarev, S. L.; Botton, G. A.; Savrasov, S. Y.; Humphreys, C. J.; Sutton, A. P., Electron-energy-loss spectra and the structural stability of nickel oxide: An LSDA+U study. *Phys. Rev. B* **1998,** 57, (3), 1505-1509.

52. Vinson, J.; Rehr, J. J.; Kas, J. J.; Shirley, E. L., Bethe-Salpeter equation calculations of core excitation spectra. *Phys. Rev. B* **2011,** 83, (11), 115106.

53. Gilmore, K.; Vinson, J.; Shirley, E. L.; Prendergast, D.; Pemmaraju, C. D.; Kas, J. J.; Vila, F. D.; Rehr, J. J., Efficient implementation of core-excitation Bethe–Salpeter equation calculations. *Comput. Phys. Commun.* **2015,** 197, 109-117.

54. Salpeter, E. E.; Bethe, H. A., A Relativistic Equation for Bound-State Problems. *Phys. Rev.* **1951,** 84, (6), 1232-1242.

55. Giannozzi, P.; Baroni, S.; Bonini, N.; Calandra, M.; Car, R.; Cavazzoni, C.; Ceresoli, D.; Chiarotti, G. L.; Cococcioni, M.; Dabo, I.; Dal Corso, A.; de Gironcoli, S.; Fabris, S.; Fratesi, G.; Gebauer, R.; Gerstmann, U.; Gougoussis, C.; Kokalj, A.; Lazzeri, M.; Martin-Samos, L.; Marzari, N.; Mauri, F.; Mazzarello, R.; Paolini, S.; Pasquarello, A.; Paulatto, L.; Sbraccia, C.; Scandolo, S.; Sclauzero, G.; Seitsonen, A. P.; Smogunov, A.; Umari, P.; Wentzcovitch, R. M., QUANTUM

ESPRESSO: a modular and open-source software project for quantum simulations of materials. *J. Condens. Matter Phys.* **2009,** 21, (39), 395502.

56. Ceperley, D. M.; Alder, B. J., Ground State of the Electron Gas by a Stochastic Method. *Phys. Rev. Lett.* **1980,** 45, (7), 566-569.

57. Perdew, J. P.; Wang, Y., Accurate and simple analytic representation of the electron-gas correlation energy. *Phys. Rev. B* **1992,** 45, (23), 13244-13249.

58. Troullier, N.; Martins, J. L., Efficient pseudopotentials for plane-wave calculations. *Phys. Rev. B Condens. Matter* **1991,** 43, (3), 1993-2006.

59. Mattei, G. S.; Dagdelen, J. M.; Bianchini, M.; Ganose, A. M.; Jain, A.; Suard, E.; Fauth, F.; Masquelier, C.; Croguennec, L.; Ceder, G.; Persson, K. A.; Khalifah, P. G., Enumeration as a Tool for Structure Solution: A Materials Genomic Approach to Solving the Cation-Ordered Structure of $Na_3V_2(PO_4)_2F_3$. *Chem. Mater*. **2020**, 32, (20), 8981-8992.

60. Shadle, S. E.; Hedman, B.; Hodgson, K. O.; Solomon, E. I., Ligand K-Edge X-ray Absorption Spectroscopy as a Probe of Ligand-Metal Bonding: Charge Donation and Covalency in Copper-Chloride Systems. *Inorg. Chem.* **1994,** 33, (19), 4235-4244.

Table of Contents